Journal of Oceanology and Limnology

https://doi.org/10.1007/s00343-025-5218-6

Research Paper

Enhancing sea ice classification on SAR imagery by integrating texture and polarimetric information with a deep learning model

Lichen GAO*

Shandong University of Science and Technology, Qingdao 266590, China

Received Jun. 18, 2025; accepted in principle Aug. 7, 2025; accepted for publication Sep. 16, 2025

Abstract The satellite synthetic aperture radar (SAR) sensor is one of the most critical tools for monitoring Arctic sea ice. Classifying sea ice types based on SAR images has been a research hotspot. Most existing deep-learning-based sea ice classification models rely on the polarimetric information of SAR images while ignoring the gray-level co-occurrence matrix (GLCM) feature. This study develops a three-branch U-Net model for classifying sea ice in SAR images. By integrating polarimetric information, GLCM features, and auxiliary data, the model can classify open water (OW), young ice (YIC), first-year ice (FYI), and old ice (OIC). The model is trained and tested on the well-known AI4Arctic sea ice challenge dataset. Experiments on 57 testing SAR images demonstrate that the proposed model achieves an overall classification accuracy of 91.45% and an Intersection over Union (IoU) of 0.846 4 for the four-type classification. Ablation experiments were conducted to evaluate the sensitivity of various GLCM features to sea ice classification. The effectiveness of the three-branch input for fusing polarimetric information, GLCM feature, and auxiliary data is validated. Results indicate that incorporating HV_mean significantly enhances classification performance, with an accuracy increase of approximately 0.7% and an improvement in IoU of 0.9%. The three-branch input structure is more effective than the single-branch structure in fusing three types of inputs, resulting in an accuracy increase of 4.7% and an improvement in IoU of 7%. Therefore, the proposed three-branch U-Net model demonstrates stable and reliable capabilities for classifying OW, YIC, FYI, and OIC in SAR images, providing a new approach for Arctic sea ice monitoring.

Keyword: synthetic aperture radar (SAR) image; sea ice classification; gray-level co-occurrence matrix (GLCM); U-Net; deep learning

1 INTRODUCTION

Arctic sea ice, a critical component of the global climate and local ecosystems (Mori et al., 2019), directly influences the balance of polar ecosystems and the safety of the Arctic maritime route due to its dynamic variability (Holland and Bitz, 2003; Zhang et al., 2021). In recent years, Arctic warming has significantly reduced both sea ice extent and thickness (Serreze and Barry, 2011; Comiso, 2012; Kwok, 2018; Rantanen et al., 2022), alongside a trend toward younger sea ice (Wang et al., 2019; Babb et al., 2023). This reduction has enhanced the navigability of Arctic shipping routes (Bi et al., 2020; Huang et al., 2021). Monitoring Arctic sea ice variability is essential for understanding interactions among sea ice, the ocean, and the atmosphere, as well as for supporting the development of Arctic maritime routes (Ye et al., 2016; Karvonen, 2017).

Satellite remote sensing technology, with its advantages of broad swath coverage and high efficiency, has become one of the primary methods for observing sea ice (Dabboor and Geldsetzer, 2014; Su et al., 2019; Dawson et al., 2022). Among these technologies, spaceborne synthetic aperture

* Corresponding author: 2057178872@qq. com; 202211030704@sdust. edu.cn

radar (SAR) provides all-weather, day-and-night imaging capabilities, making it widely used in sea ice remote sensing monitoring (Fetterer et al., 1997; Soh and Tsatsoulis, 1999; Dabboor and Geldsetzer, 2014; Wang et al., 2016; Zhang et al., 2016; Radhakrishnan et al., 2021; Qu and Su, 2023).

Sea ice can be categorized by developmental stage into open water (OW), new ice (NIC), young ice (YIC), thin first-year ice (FYI-t), thick first-year ice (FYI-T), and old ice (OIC) (Comiso, 1990; Li et al., 2024). New ice typically has a thickness of less than 10 cm, YIC ranges from 10 to 30 cm, FYI-t measures 30 to 70 cm, FYI-T usually exceeds 70 cm, and OIC often surpasses 200 cm (Park et al., 2020). Due to the similarity in spectral or textural characteristics of remote sensing images, the six sea ice classes are generally consolidated into four primary categories: OW, YIC, FYI, and OIC (Chen et al., 2025). Efficient and safe polar maritime transportation depends on real-time, accurate information about sea ice types. SAR enables the collection of high-resolution sea ice distribution data, facilitating the monitoring of Arctic sea ice dynamics. Therefore, SAR-based sea ice classification is crucial for ensuring the safety of polar navigation and analyzing changes in sea ice (Walker et al., 2006; Zhang et al., 2013; Geldsetzer et al., 2023).

Researchers have conducted extensive studies on sea ice classification using SAR imagery, which can generally be categorized into three stages. The first stage focuses on expert systems, with Advanced Reasoning using Knowledge for Typing Of Sea ice (ARKTOS) being a prominent example. ARKTOS (Soh et al., 2004) employs an enhanced watershed merging algorithm to perform adaptive segmentation on preprocessed RADARSAT imagery. It computes 25 feature attributes for each segmented region, including average intensity, contrast, spatial relationship features, and texture features, among others. These features are then used to classify the imagery into OW, YIC, FYI, and OIC. By leveraging region-based features and rule-based reasoning, ARKTOS demonstrates superior performance compared to most pixel-based feature models.

The second stage mainly relies on machine learning (ML) methods, with representative techniques including support vector machine (SVM), random forest (RF), and neural network (NN). Zakhvatkina et al. (2013) employed a NN model that combined backscatter imagery and gray-level co-occurrence matrix (GLCM) features to classify OIC, FYI, and OW in SAR imagery. Liu et al. (2015) similarly utilized GLCM features to develop an SVM classification model using RADARSAT-2 dual-polarization data. Their approach achieved an overall accuracy of 91% on 6 250 test samples in the Beaufort Sea, significantly outperforming conventional maximum likelihood classification methods. Park et al. (2019) trained a model for sea ice classification using RF on Sentinel-1 dual-polarization SAR images, replacing manual annotations with ice charts from the National Snow and Ice Data Center (NSIDC). The model achieved an accuracy of 85% for classifying OW, FYI, and MYI, while the accuracy for distinguishing OW from the four sea ice types reached 58%.

The third stage is the deep-learning-based sea ice classification (Cui et al., 2020; Li et al., 2020; Xu and Ren, 2021; Gao et al., 2022; Li and Wang, 2023; Wang and Li, 2024a). Traditional ML methods rely on complex feature engineering from raw SAR images, which limits their classification accuracy. The deep learning model can learn features from raw data, showcasing strong feature extraction capabilities (Reichstein et al., 2019; Li et al., 2020; Wang and Li, 2024b). Ren et al. (2022) developed a pixel-level classification framework based on the U-Net model for dual-polarization SAR images. The model employs ResNet-34 as the encoder and utilizes both the position attention module (PAM) and the channel attention module (CAM). Huang et al. (2024) proposed a DBU-Net sea ice classification model that combines polarimetric information with GLCM features. Their dual-branch architecture effectively fused these distinct classification bases, demonstrating improved accuracy over the original U-Net and yielding more precise classification results (Huang and Ren, 2023). Chen et al. (2024) and Jiang et al. (2024) enhanced the U-Net model by integrating multiple data sources, including SAR image, AMSR2 (6.9–36.5 GHz) data, and ERA5 weather data, while optimizing the loss function to improve classification performance. Chen et al. (2025) further proposed a weakly supervised learning approach that utilizes low-resolution polygon labels for training. By optimizing the U-Net model with polygon-based loss functions, this method achieved higher classification accuracy than the fully supervised benchmark, demonstrating particularly significant improvements in distinguishing YIC from OIC. The effectiveness of auxiliary data inputs was also validated.

Currently, deep learning-based sea ice classification methods can significantly improve the accuracy and

efficiency of sea ice classification in SAR images, making them the mainstream technical approach in this field. Previous studies have demonstrated the effectiveness of GLCM features in sea ice detection (Su et al., 2013) and sea ice classification (Soh and Tsatsoulis, 1999; Liu et al., 2015). The GLCM feature can effectively characterize the texture features of SAR images (Lohse et al., 2021). However, its computation involves non-differentiable processes, which makes it incompatible with the backpropagation learning mechanism of deep neural networks. The DBU-Net deep learning model (Huang et al., 2024) has demonstrated that explicitly incorporating the GLCM feature enhances classification accuracy between FYI and OIC. However, to achieve more refined sea ice classification, such as distinguishing among OW, YIC, FYI, and OIC, will the inclusion of GLCM feature input provide further improvements?

To address this issue, we propose a three-branch input U-Net model for fine-grained sea ice classification in SAR images, which integrates both polarimetric information and the GLCM feature to distinguish among four sea ice types: OW, YIC, FYI, and OIC. The model receives three inputs: SAR image polarimetric data, GLCM features, and auxiliary information. It encodes and fuses these input features before feeding them into the U-Net framework, ultimately achieving four-class classification in SAR images.

The model is trained and validated using the well-known AI4Arctic Sea Ice Challenge Dataset (Stokholm et al., 2024). Ablation experiments are conducted to assess the sensitivity of various GLCM features to sea ice classification. The experiments demonstrate that GLCM features, specifically the Mean feature of Horizontal Transmit, Vertical Receive polarization (HV-polarized) images (HV_mean), significantly enhance classification accuracy, achieving improvements of 4.7% and 7% in precision and Intersection over Union (IoU), respectively. Additionally, comparative experiments were designed to explore fusion strategies for polarimetric information, auxiliary data, and the GLCM feature, confirming that the proposed three-branch input strategy is effective.

This paper is organized as follows: Section 2 describes the dataset; Section 3 details a Three-Branch Input U-Net Sea Ice Classification Model Incorporating GLCM feature; Section 4 presents comparative experiments analyzing the sensitivity of different GLCM features to sea ice classification and the impact of fusion strategies on model performance; and Section 5 provides concluding remarks.

2 DATA

2.1 SAR imagery and label

The AI4Arctic Sea Ice Challenge dataset is a well-known open dataset comprising 533 SAR images that document sea ice thermodynamic processes and hydrosphere interactions across the Canadian Arctic and Greenland coastal regions from 2018 to 2021. Each training file integrates four geospatial data modalities: dual-polarized Sentinel-1 Extra Wide (EW) swath images and auxiliary data. The auxiliary data include Advanced Microwave Scanning Radiometer 2 (AMSR2) passive microwave radiometer measurements and numerical weather prediction (NWP) parameters from the ERA5 reanalysis dataset, including AMSR2 brightness temperatures (Dual-pol AMSR2 brightness temperature data in 18.7 and 36.5 GHz), environmental variables (10-m wind speed, 2-m air temperature, total column water vapor, total column cloud liquid water), and spatiotemporal metadata (latitude/longitude of each pixel and scene acquisition month), which provide auxiliary classification information beyond SAR polarimetric characteristics (Chen et al., 2024).

The sea ice labels in the AI4Arctic Sea Ice Challenge dataset originate from expert visual interpretation and manual delineation conducted by the Danish Meteorological Institute (DMI) and Canadian Ice Service (CIS), following the World Meteorological Organization (WMO) SIGRID-3 standard. These annotations employ a vector polygon encoding system to record dominant ice types within each region. To accommodate deep learning requirements, the AI4Arctic Sea Ice Challenge research team has professionally reconstructed the original SIGRID-3 encoding scheme. Through analysis of Arctic sea ice distribution characteristics, the 23 original developmental stage codes were consolidated into six physically meaningful categories: OW, NIC, YIC, FYI-t, FYI-T, and OIC. This classification system preserves critical ice thickness thresholds while effectively mitigating model overfitting caused by small-sample categories. Based on the similarity of spectral and textural features, these six categories were further aggregated into four primary classification types: OW, YIC, FYI, and OIC. Figure 1 demonstrates representative SAR images and their corresponding label images from the AI4Arctic Sea Ice Challenge dataset.

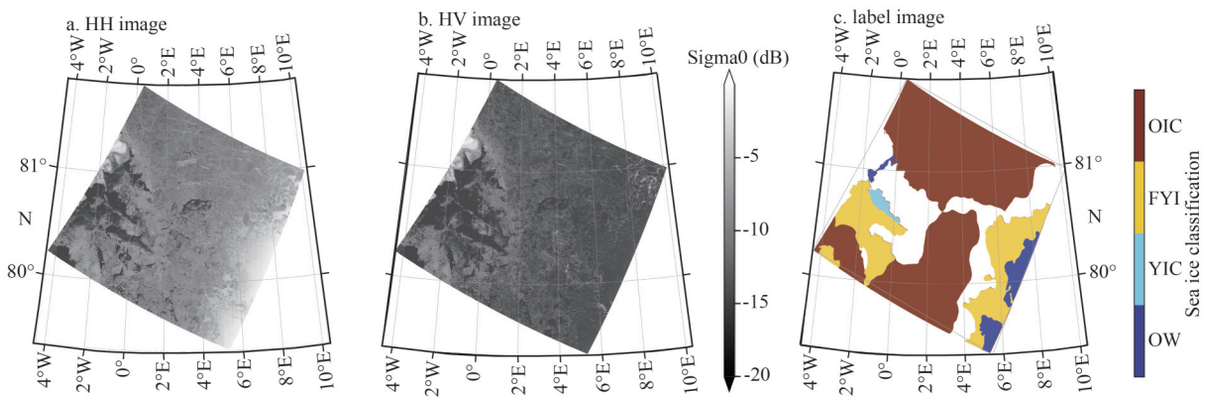

Fig.1 Example of a SAR image and a label image

White areas represent land masses, unlabeled ocean zones, and regions with uncertain sea ice types as determined by expert systems.

The study employs the officially provided ready-to-train dataset version, where the original 40-m resolution SAR imagery was downsampled to an 80-m resolution using a 2×2 Gaussian kernel. To address the nonlinearity of SAR backscatter coefficients, the dual-channel HH/HV data were normalized to the [-1, 1] range through per-channel min-max scaling while retaining the incidence angle data to enable the model to learn its influence on polarimetric information automatically. NaN pixels in the SAR channels were replaced with zeros, and ice mask values were encoded as 255 to exclude invalid regions from loss computation. All auxiliary data, including AMSR2 brightness temperature measurements (Zhao et al., 2023) and ERA5 meteorological parameters (Hersbach et al., 2020), were resampled to match the resolution of the SAR image. Moreover, the dataset includes supplementary information, such as acquisition time (month) and latitude/longitude grid coordinates of SAR observations, as additional auxiliary data. For experimental validation, the study uses 451 scenes from the ready-to-train dataset for training and 57 unique scenes for testing, ensuring no overlap between the training and test sets. The reasons for selecting the 57 testing scenes include: (1) the training set must encompass all classes, with each class containing a statistically significant number of samples; (2) the dataset shall include complete coverage of all 12 calendar months to characterize the complete seasonal cycle; (3) deliberately increase sampling in the marginal ice zone to enhance the model's capability in discriminating complex boundaries.

2.2 GLCM feature

The GLCM features were computed using the SNAP software with the following parameter configurations: A 9×9 window size was selected to balance local texture details with computational efficiency. The angular parameter was set to "ALL" (averaging results across 0°, 45°, 90°, and 135° directions) to achieve orientation-invariant texture analysis. The probability quantizer mapped gray values to 32 discrete levels to preserve essential texture information, while a displacement of 4 pixels was adopted to capture medium-scale texture patterns. Invalid pixels containing no-data values (-9 999.0) were systematically excluded from the computation.

To investigate the independent contributions of various GLCM feature to sea ice classification, this study performed an inter-class separability analysis for 10 GLCM feature (including entropy, variance, mean, etc.) under both HH and HV polarizations. The Jeffries-Matusita (JM) distance was selected as the separability metric (Sen et al., 2019). Among the extracted features, five GLCM features—entropy, variance, mean, homogeneity, and contrast—demonstrated significant discriminative capabilities for distinguishing between YIC, FYI, and OIC. For illustrative purposes, we selected three GLCM features with the highest JM distances as representative examples. Figure 2 presents the distribution of these three GLCM features across different sea ice types under both polarizations, revealing notable differences in their discriminative performance. For HH-polarized-based parameters, HH_entropy showed relatively consistent but limited classification capability, with JM values uniformly distributed in the 0.13–0.39 range, indicating stable but unremarkable separability across ice types. The particularly low JM value (0.132 6) for the FYI_OIC pair suggests poor performance in distinguishing ice age

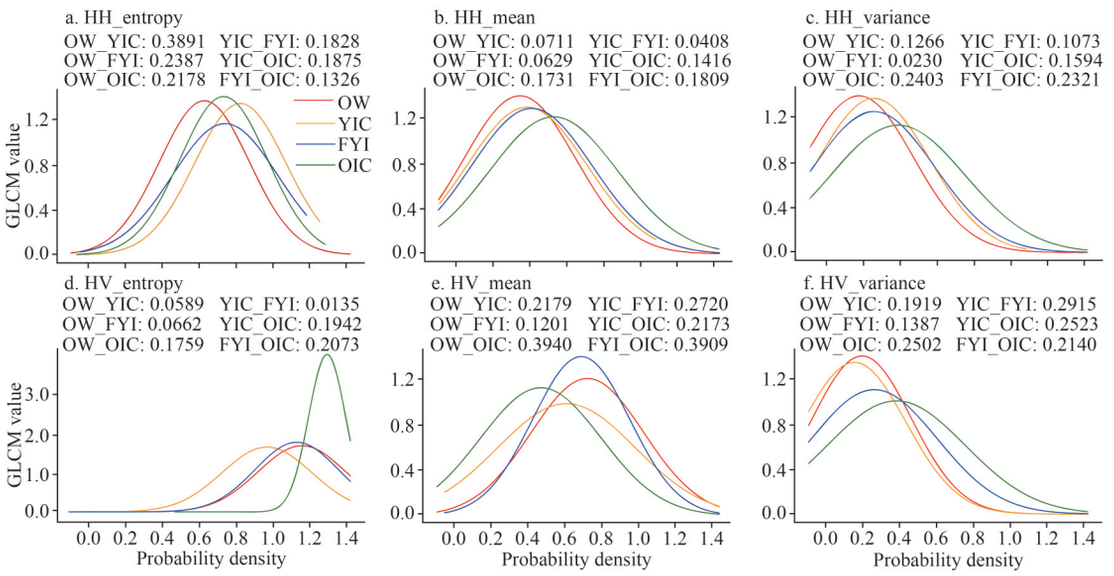

Fig.2 Sea ice type distribution of entropy, mean, and variance features

The text above each subplot display the corresponding JM distance values for different sea ice types (OW, YIC, FYI, OIC).

differences. HH_variance exhibited moderate improvement over mean values but remained limited in overall discriminative power. Both HH_mean and HV_entropy demonstrated weak classification performance, with most JM values below 0.1. In contrast, HV_mean and HV_variance maintained consistently high JM values (0.2–0.4 range) across all three ice types (FYI/YIC/OIC). HV_mean demonstrated strong performance in critical combinations: OW_OIC (JM=0.394 0) and FYI_OIC (JM=0.390 9), indicating effectiveness for both ice type discrimination and OW detection. HV_mean slightly surpassed the HV_variance in distinguishing OW (e.g., OW_YIC: HV_mean= 0.217 9>HV_variance=0.191 9).

3 A THREE-BRANCH INPUT U-NET SEA ICE CLASSIFICATION MODEL INCORPORATING GLCM FEATURE

3.1 The architecture of the proposed model

As illustrated in Fig.3, the enhanced three-branch U-Net architecture with the GLCM feature has four primary components: input, encoder, decoder, and output, with nearly symmetric configurations between the encoder and decoder. The model includes three independent input branches that process SAR polarimetric data, the GLCM feature, and auxiliary data, respectively. Multi-source information fusion is accomplished through channel concatenation and 3×3 convolution operations. The input image size is

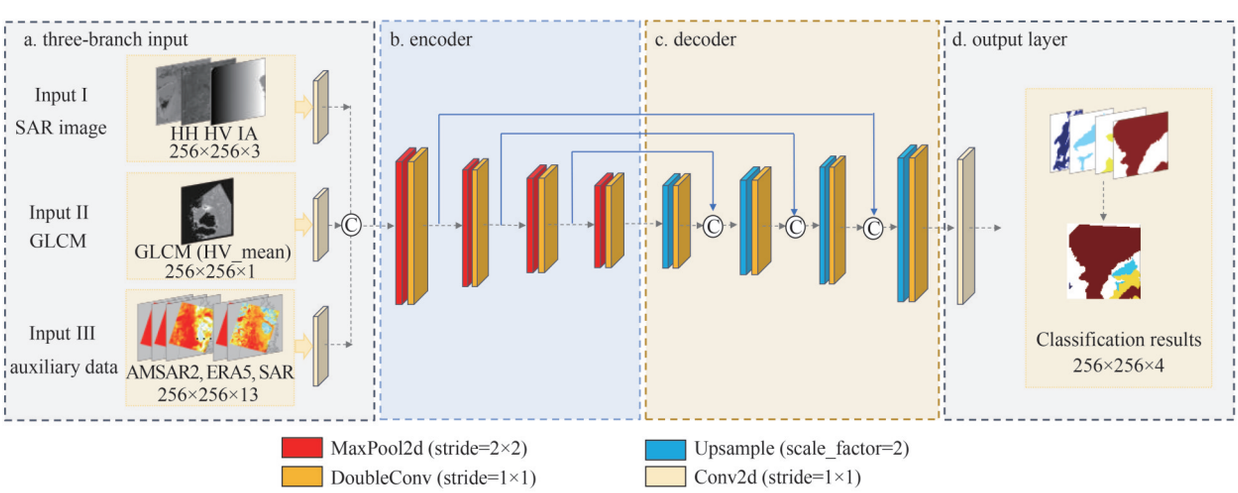

Fig.3 Three-branch input U-Net sea ice classification model incorporating GLCM feature

standardized to 256×256 pixels. The encoder employs a four-level downsampling structure to compress spatial dimensions and progressively extract multi-scale abstract features. The decoder applies bilinear interpolation, upsampling, and skip connections to merge encoder features, gradually restoring resolution to the original dimensions via dual convolution operations, ultimately generating the sea ice classification results through the output layer. The subsequent sections elaborate on the encoder, decoder, and output components of this model.

3.1.1 Three-branch input

The U-Net model achieved the best performance in the AutoICE challenge, which demonstrates its superior capability in this specific task. Therefore, we select U-Net as our baseline model for further optimization (Gillioz et al., 2020; Alkaee Taleghan et al., 2025). The proposed three-branch input U-Net model adopts a cross-modal convolutional fusion strategy to process multi-source remote sensing data. Three parallel input branches handle distinct data types: (1) 3-channel polarimetric SAR data (HH image, HV image, and incidence angle (IA) information); (2) 1-channel GLCM feature; and (3) 13-channel auxiliary inputs (including geometrically calibrated and resampled AMSR2 brightness temperature data, ERA5 meteorological parameters, as well as SAR observation timestamps and geolocation grid information). Each branch first undergoes feature extraction through an independent dual-convolution module, which employs 3×3 convolutional kernels combined with batch normalization and rectified linear unit (ReLU) activation functions, transforming each data modality into a unified feature representation space while maintaining spatial resolution. The feature maps from all three branches are then concatenated along the channel dimension to form a composite feature tensor. To optimize feature fusion, the model incorporates a critical 3×3 fusion convolution layer that automatically adjusts the contribution weights of different branch features through learnable parameters, generating information-rich fused feature representations while preserving spatial consistency. This approach provides a robust foundation for features in downstream tasks. The model employs CrossEntropyLoss as the loss function. Since CrossEntropyLoss inherently combines the softmax operation and negative log likelihood loss computation, no explicit softmax activation function is added to the output layer.

3.1.2 Encoder

The encoder employs a four-level cascaded downsampling structure to achieve multi-scale information fusion through hierarchical feature extraction. Each downsampling module first applies 2×2 max-pooling layers to spatially compress the input feature maps, progressively reducing the resolution from 256×256 pixels to 32×32 pixels. Along the channel dimension, feature reorganization is achieved through dual-convolution modules, with the number of channels increasing according to the predefined sequence [32, 32, 64, 64]. Each dual-convolution module consists of two consecutive 3×3 convolutional layers, each followed by 2D batch normalization and rectified linear unit (ReLU) activation. The ReLU activation function helps mitigate gradient vanishing and explosion issues during model training. The bridge layer, designed as the core output of the fourth-level downsampling, adopts the same 64-channel structure as the third level, achieving feature compression and deepening through an additional ContractingBlock. The encoder outputs 16×16×64 feature maps that serve as input sources for the decoder.

3.1.3 Decoder

The decoder adopts a four-level upsampling structure that is symmetric to the encoder. Each decoding module receives inputs from both the previous decoder output and the corresponding encoder feature maps at the same level. This fusion approach fully utilizes the feature maps extracted by the encoder while minimizing information loss. At each level, the feature map resolution is initially doubled through bilinear interpolation upsampling, with dynamic padding ensuring spatial dimension alignment before channel concatenation. The concatenated feature maps then undergo feature fusion through dual-convolution modules, which comprise two 3×3 convolution operations, followed by batch normalization and ReLU activation. The decoder produces output feature maps with a resolution of 256×256×32.

3.1.4 Output layer

The final decoder output feature maps are processed through a dedicated 1×1 convolutional layer with a stride of 1, where the number of filters equals the number of sea ice categories. This configuration enables the generation of pixel-wise classification results through segmentation.

3.2 Training specification

The detailed specifications for model training are

presented in Table 1. The learning rate scheduling employs PyTorch's CosineAnnealingLR scheduler, initialized at 0.000 1 and smoothly decayed to a minimum of 0 through cosine annealing, combined with the SGD optimizer (momentum=0.9, weight decay=0.01) to ensure stable convergence. The cross-entropy loss function (CrossEntropyLoss) is implemented with ignore_index=255 to exclude invalid pixels from the computation.

During training, each epoch consists of 500 iterations with a batch size of 16. The data augmentation strategy incorporates only random horizontal and vertical flipping (with a 50% probability for each) without employing more complex transformations such as rotation or scaling. To prevent overfitting, an early stopping mechanism halts training when the validation loss shows no improvement for 30 consecutive epochs. For assessing model generalization, each experiment randomly selects 10 SAR images from the training data to serve as a validation set. Model selection is based on the F1-scores metric evaluated on this validation set, with optimal parameters automatically saved for subsequent predictions on test data. The entire training process utilizes mixed-precision acceleration and model compilation optimization to enhance computational efficiency.

4 MODEL TESTING AND ANALYSIS

4.1 Sensitivity experiment for a single GLCM feature

To evaluate the impact of a single GLCM feature on classification performance, we conducted sensitivity tests by independently inputting five GLCM features—entropy, variance, mean, contrast, and homogeneity—from different polarization channels (HH and HV) into the three-branch U-Net model. The objective was to assess their influence on overall classification accuracy and per-class performance (OW, YIC, FYI, OIC). The results are presented in Table 2 and illustrated in Fig.4. For clarity, we selected the six results with the top metrics to display. Therefore, we highlight in the confusion matrix three more discriminative features with superior classification results: mean, entropy, and variance, which exhibit higher precision and IoU values. Table 2 presents the precision and IoU metrics for different GLCM features (HH_entropy, HH_variance, HH_mean, HV_entropy, HV_variance, HV_mean), while Fig.4 illustrates the confusion matrices obtained during model training.

As shown in Fig.4b and Table 2, HV_mean demonstrated superior performance in the four-class sea ice classification task, achieving the highest precision (0.914 5) and IoU (0.846 4). Notably, it exhibited stable classification accuracy across YIC (0.78), FYI (0.86), and OIC (0.92), indicating its robustness in capturing textural differences among ice types. However, HV_mean significantly reduced misclassification between YIC and FYI (Fig.4b). In contrast, HH_entropy showed moderate performance in classifying FYI but suffered from severe misclassification of YIC (Fig.4c). In summary, HV_mean demonstrated superior classification accuracy across all four ice categories (Fig.4b).

To further validate these findings, we selected a representative SAR image to visualize the classification results. As illustrated in Fig.5c, HV_mean exhibits significant advantages in distinguishing between YIC and FYI, showing strong consistency with the

Table 1 Model training parameters

Optimizer	SGD
Learning rate	0.000 1
Weight decay	0.01
Scheduler	CosineAnnealingLR
Batch size	16
Number of iterations per epoch	500
Momentum	0.9
Downscaling ratio	10
Patch size	256
Number of validation scenes	10
Number of cross-validation runs	20
Number of testing scenes	57
Early_stopping_patience	30

Table 2 Accuracy evaluation results for single GLCM feature sensitivity tests

GLCM	Precision	IoU
HH_mean	0.904 5	0.831 4
HV_mean	**0.914 5**	**0.846 4**
HH_entropy	0.899 2	0.825 1
HV_entropy	0.902 2	0.829 1
HH_variance	0.894 9	0.818 7
HV_variance	0.912 9	0.845 4
HH_constrast	0.877 3	0.791 9
HV_constrast	0.865 2	0.774 2
HH_ homogeneity	0.873 9	0.786 4
HV_ homogeneity	0.869 9	0.782 3

Bold shows the best performance among all GLCM features (HV_mean with precision 0.914 5 and IoU 0.846 4).

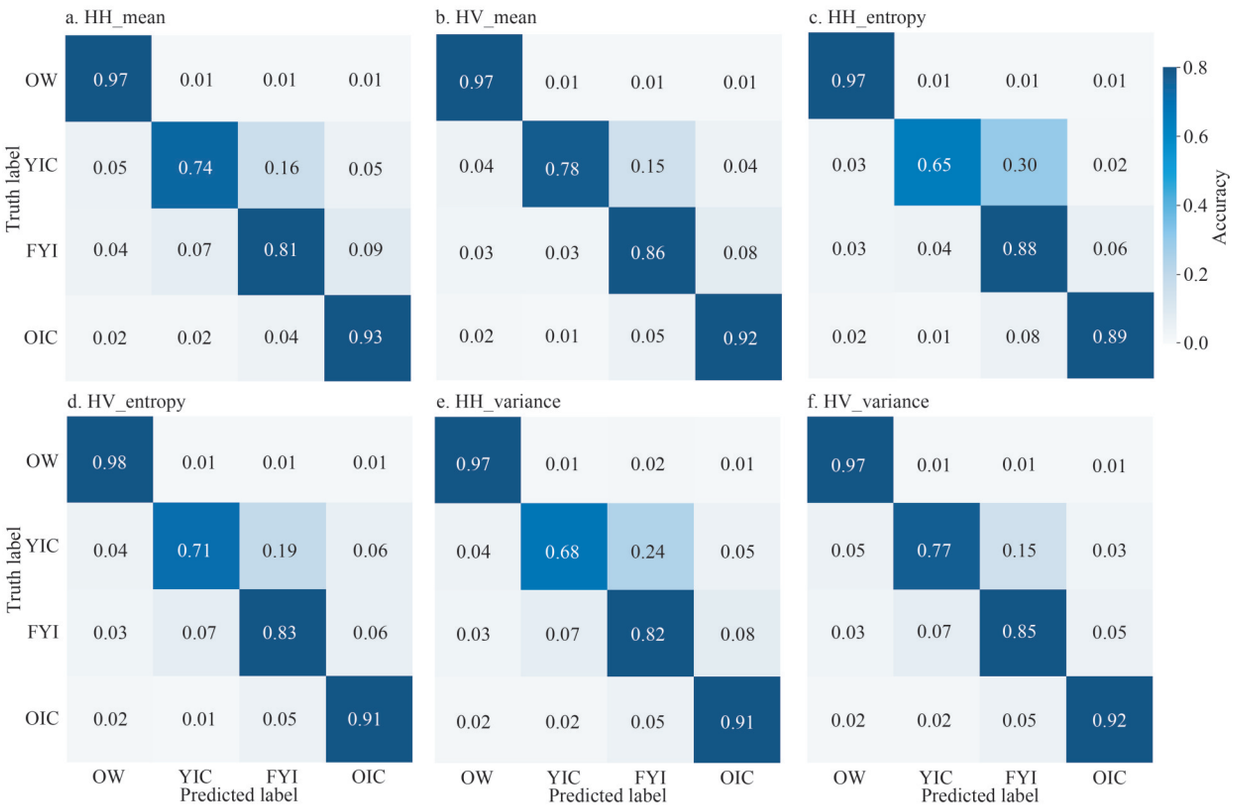

Fig.4 Confusion matrices for single GLCM feature sensitivity tests

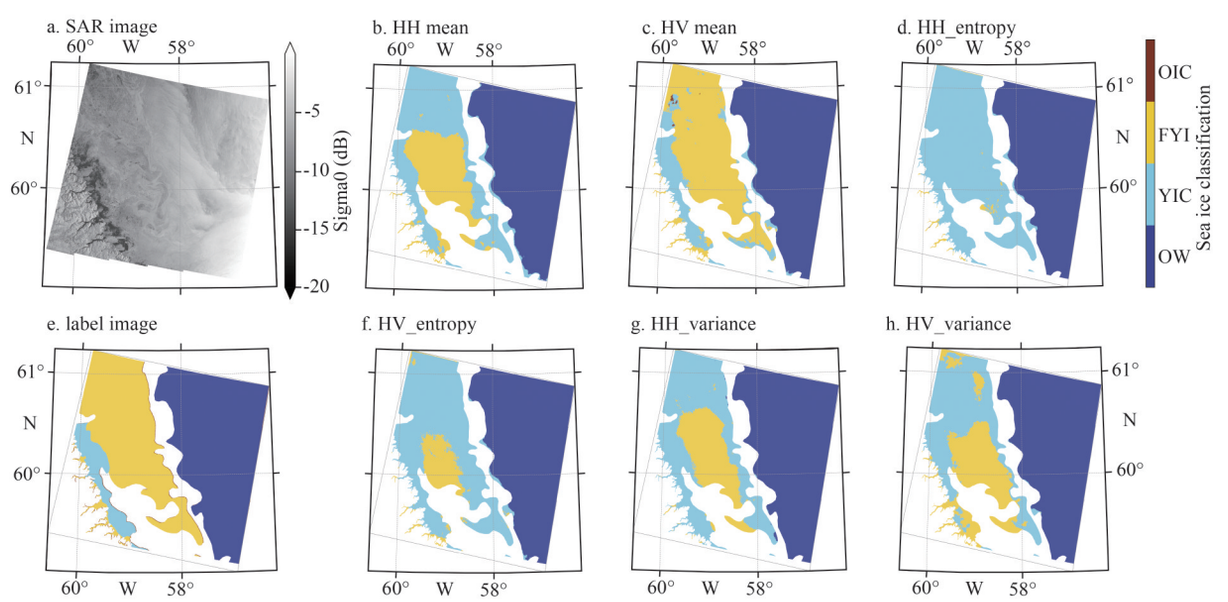

Fig.5 Classification results of single GLCM feature sensitivity tests for scene 20200217T102731_cis

ground truth labels (Fig.5e), with a classification performance that is markedly better than that of other GLCM features under different polarizations. Although minor misclassifications persisted, the overall separation between ice types was significantly improved, with minimal overlap or confusion.

4.2 Sensitivity experiment for multiple GLCM features

Given that the single GLCM feature, HV_mean, improves classification accuracy, we explore whether stacking multiple GLCM features could bring further improvements. However, as many feature

pairs were known to be highly correlated, their simultaneous inclusion would lead to computational redundancy without proportional accuracy improvement. Based on the five single features, we design thirteen feature combinations and test the performance of each combination. To concisely display the results, we present the six combinations with the highest metrics in Table 3 and Fig.6.

The results revealed that while certain combinations (e.g., HHHV_mean+HHHV_variance) improved robustness for specific classes (e.g., FYI shown in Fig.6c), none achieved a balanced enhancement across all four ice types. Notably, multi-feature combinations did not surpass the performance of HV_mean (precision: 0.914 5, IoU: 0.846 4). Some combinations even introduced computational redundancy without proportional gains in accuracy. Therefore, stacking multiple GLCM feature does not yield improvements greater than those of HV_mean in the four-type sea ice classification. The deep learning architecture is not the primary reason. The calculation of GLCM feature contains non-differentiable procedures. Since deep learning relies on backpropagation and gradient-based optimization, the non-differentiable nature of GLCM feature makes it difficult for the deep learning model to learn the textural information by itself. This is also why we fed the GLCM feature to the model as a raw input.

Table 3 Accuracy evaluation results for multiple GLCM feature sensitivity tests

GLCM	Precision	IoU
HHHV_mean	0.894 3	0.817 6
HHHV_entropy+HHHV_mean	0.900 1	0.824 1
HHHV_mean+HHHV_variance	0.905 4	0.838 3
HHHV_entropy+HHHV_mean+HHHV_variance	0.897 7	0.822 0
HH_entropy+HH_mean+HH_contrast+HH_homogeneity	0.879 5	0.793 9
HH_mean+HH_contrast+HH_homogeneity	0.882 2	0.796 0

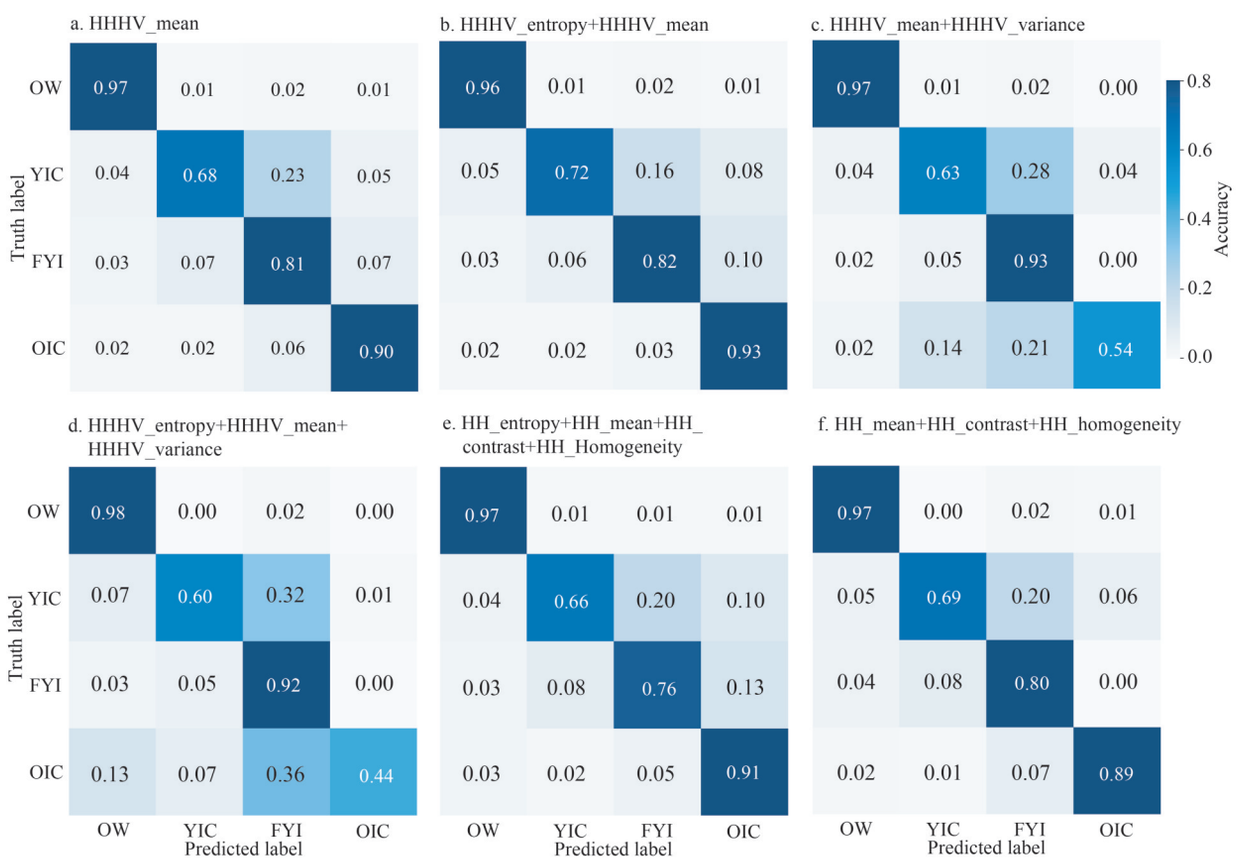

Fig.6 Confusion matrices for multiple GLCM feature sensitivity tests

4.3 Evaluation experiment for the three-branch structure

To evaluate the efficiency of the proposed three-branch structure for fusing polarimetric information, GLCM feature, and auxiliary data, we designed four comparative experiments: (1) a baseline U-Net using only polarimetric SAR data and auxiliary inputs; (2) a single-branch U-Net incorporating polarimetric data, auxiliary inputs, and HV_mean; (3) a dual-branch U-Net where the first branch processes polarimetric SAR data and auxiliary inputs while the second branch handles HV_mean; (4) a three-branch U-Net with dedicated branches for polarimetric SAR data, HV_mean, and auxiliary data, respectively; (5) DeeoLabv3 incorporating polarimetric data, auxiliary inputs, and HV_mean; (6) Swin Transformer incorporating polarimetric data, auxiliary inputs, and HV_mean. Table 4 presents the metrics, and Fig.7 displays the confusion matrices.

The baseline U-Net exhibits inferior performance compared to other architectures across all four evaluation metrics (precision, recall, F1-score, and IoU), as shown in Table 4. Figure 7a shows that the baseline U-Net model exhibits significant confusion between YIC and FYI classifications. The single-branch U-Net, which incorporates HV_mean, demonstrates a notable improvement in YIC classification accuracy, confirming the discriminative capability of HV_mean for YIC classification. However, this improvement remains limited, as evident in Fig.7b, where persistent confusion between YIC and FYI persists. The dual-branch U-Net employs a two-path architecture that combines polarimetric data with auxiliary data in one branch while processing HV_mean in the other. It results in a minor decrease in IoU. As illustrated in Fig.7c, the

Table 4 Accuracy evaluation results for different network architectures

Model	Precision	IoU
Baseline U-Net	0.867 5	0.776 4
Single-branch U-Net	0.874 6	0.785 5
Sual-branch U-Net	0.873 3	0.784 4
Three-branch U-Net	**0.914 5**	**0.846 4**
DeepLabv3	0.863 4	0.768 6
Swin Transformer	0.885 9	0.800 8

Bold shows the best performance among all network architectures (three-branch U-Net with precision 0.914 5 and IoU 0.846 4).

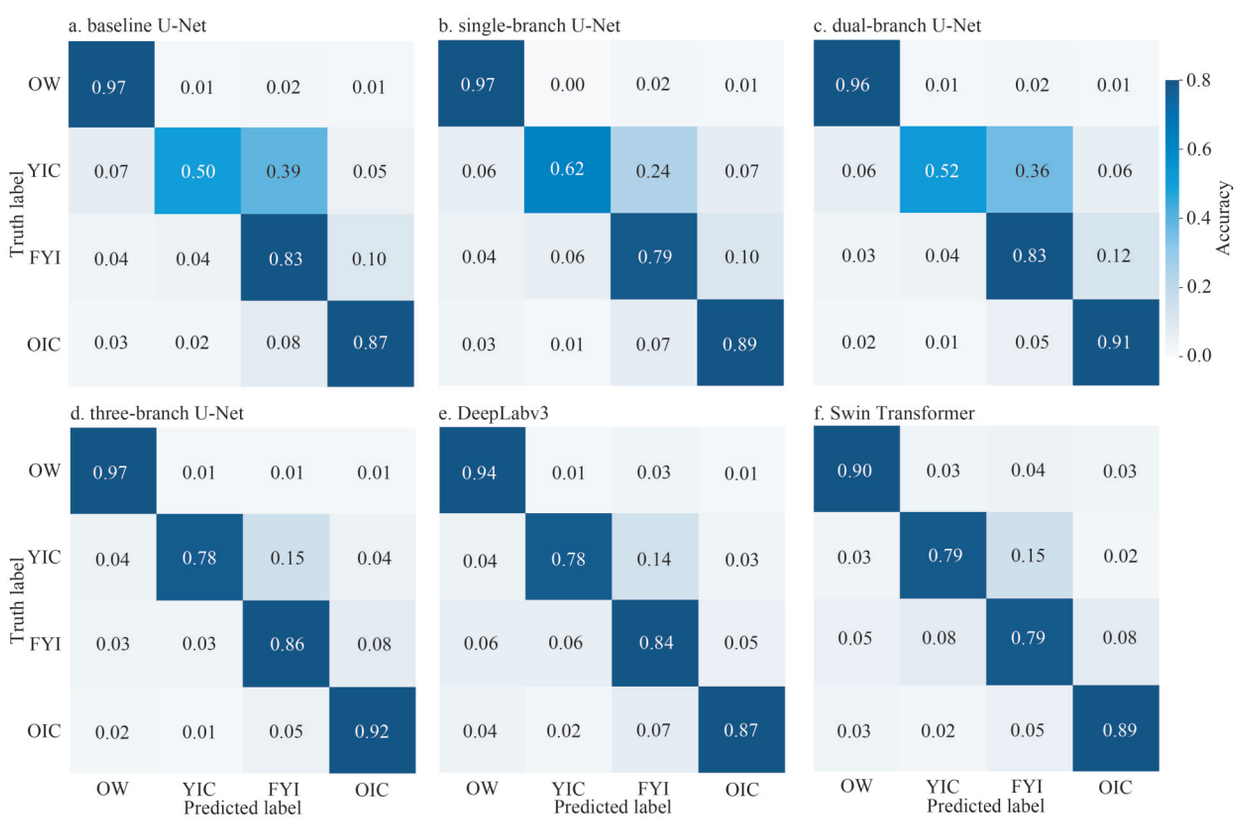

Fig.7 Confusion matrices for different network architectures

model still maintains a relatively high misclassification rate between YIC and FYI. These findings suggest that the dual-branch feature fusion strategy fails to exploit the discriminative potential of HV_mean fully.

Compared with the aforementioned two models, the three-branch U-Net demonstrates significant improvements across all evaluation metrics (Table 4). Notably, it achieves a 7% increase in IoU compared to the baseline model. These results confirm that the three-branch input model, which separately processes polarimetric information, auxiliary data, and HV_mean before feature fusion, effectively leverages the respective advantages of these three data types. In terms of sea ice classification performance, the model maintains high accuracy for both OW and OIC, with IoU scores exceeding 0.9. Simultaneously, it shows remarkable improvement in classifying YIC and FYI, reducing their cross-misclassification rates below 0.15 (Fig.7d). The performance improvement can be attributed to the design of the three-branch architecture, which first extracts features independently from each of the three input types before performing high-level feature fusion. Compared to the DeepLabv3 (Fig.7e) and Swin Transformer (Fig.7f) models, the YIC classification performs comparably to the three-branch U-Net. However, its accuracy in the three categories—OW, MYI, and OIC—is slightly lower than that of the three-branch U-Net. The three-branch U-Net effectively achieves complementary integration of multimodal input information, thereby enhancing classification accuracy for four-type sea ice identification in SAR images.

To systematically evaluate model performance, we selected multiple sets of 256×256-pixel sample slices for visual analysis. As shown in Fig.8, each comparison group sequentially displays the following: the SAR image, label, along with prediction results from six models—baseline U-Net, single-branch improved U-Net, dual-branch U-Net, three-branch U-Net, DeepLabv3, and Swin Transformer. This side-by-side comparison provides an intuitive demonstration of performance differences among models in terms of detail preservation and classification accuracy.

The results of the three-branch U-Net not only achieve higher accuracy in sea ice classification but also produce more natural gradations in transition zones between categories, with some segmented slices nearly matching the label images.

Furthermore, we select three representative images to visually compare the performance of the aforementioned models, shown in Figs.9–11.

The SAR image in Fig.9a contains OW, YIC, and FYI. The baseline U-Net exhibits two critical classification errors (Fig.9c): (1) extensive misclassification of YIC along ice-water boundaries and (2) significant cross-category confusion between FYI and YIC, consistent with the category mixing issues described in Section 4.3. While the single-branch enhanced U-Net reduces OW misclassification (Fig.9d), it still produces blurred transitional zones between FYI and YIC. This result suggests that the simple feature fusion approach lacks sufficient discriminative capability for precise ice-type delineation. The dual-branch U-Net shows expanded confusion regions between FYI and YIC compared to the baseline (Fig.9e), suggesting potential limitations in its multi-input fusion strategy. The sea ice type prediction results from DeepLabv3 and Swin Transformer models are generally consistent with the label images; however, minor misclassifications still occur, particularly at sea ice margins and transition regions between different ice types (Fig.9g–h). In contrast, the three-branch U-Net demonstrates superior classification performance (Fig.9f), exhibiting sharply defined ice-water boundaries with minimal errors in water classification. The model establishes a clear demarcation between FYI and YIC regions while achieving substantially reduced cross-category misclassification rates compared to the baseline model.

The SAR image shown in Fig.10a primarily consists of OIC with interspersed FYI and minor OW regions. As demonstrated in the baseline U-Net, single-branch U-Net, dual-branch U-Net, and DeepLabv3, all misclassify OIC boundary regions as OW, while generating fragmented OIC artifacts (Fig.10c–e). In comparison, the three-branch U-Net achieves superior classification accuracy (Fig.10f), exhibiting the closest agreement with ground truth labels. This model eliminates OW misclassification while producing sharper, more continuous OIC boundaries. Additionally, it significantly reduces internal OIC fragmentation artifacts.

The SAR image in Fig.11a contains all four sea ice categories. As shown in Fig.11c, d, e, and g, the baseline U-Net, single-branch U-Net, dual-branch U-Net, and DeeoLabv3 have insufficient feature learning capabilities, resulting in extensive misclassification of FYI regions as OW, YIC, and OIC. In contrast, while the three-branch U-Net still exhibits partial FYI misclassification (Fig.11f), its results show the closest agreement with the ground truth labels. The model produces clearly defined boundaries with superior spatial continuity while achieving higher classification accuracy for OW compared to the

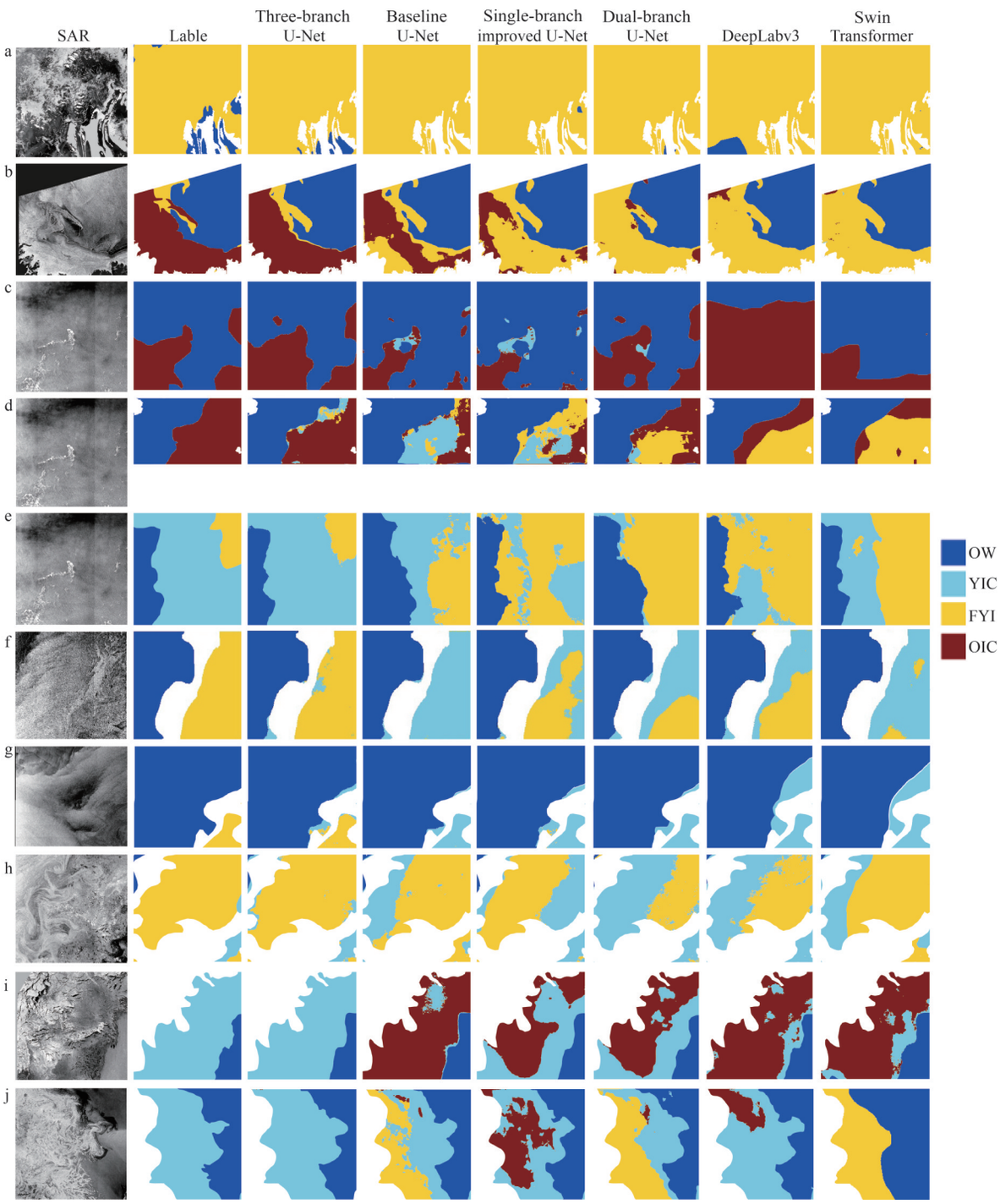

Fig.8 Visual comparison of 2 048×2 048-pixel sample slices showing (from left to right): SAR image, label, Baseline U-Net, single-branch improved U-Net, dual-branch U-Net, three-branch U-Net, DeepLabv3, and Swin Transformer

other three architectures.

As shown in Figs.10–11, while both the three-branch U-Net and Swin Transformer produce prediction results that visually closely resemble labels, the three-branch U-Net demonstrates superior performance in precision and IoU. Furthermore, it exhibits more robust and stable classification capabilities for OW, MYI, and OIC, conclusively validating the superiority of the three-branch U-Net architecture. In summary, the three-branch input U-Net sea ice classification model proposed in this paper effectively fuses polarimetric information, auxiliary information, and GLCM feature information in SAR images through innovative architecture

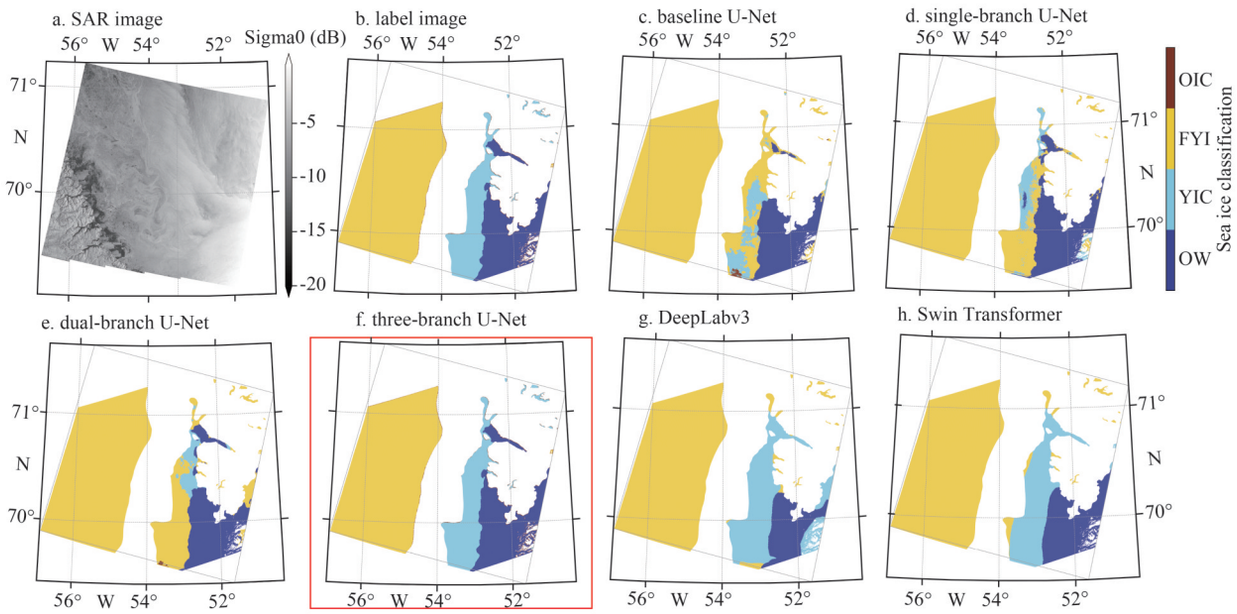

Fig.9 Classification results of different network architectures for scene 20210129T103213_dmi

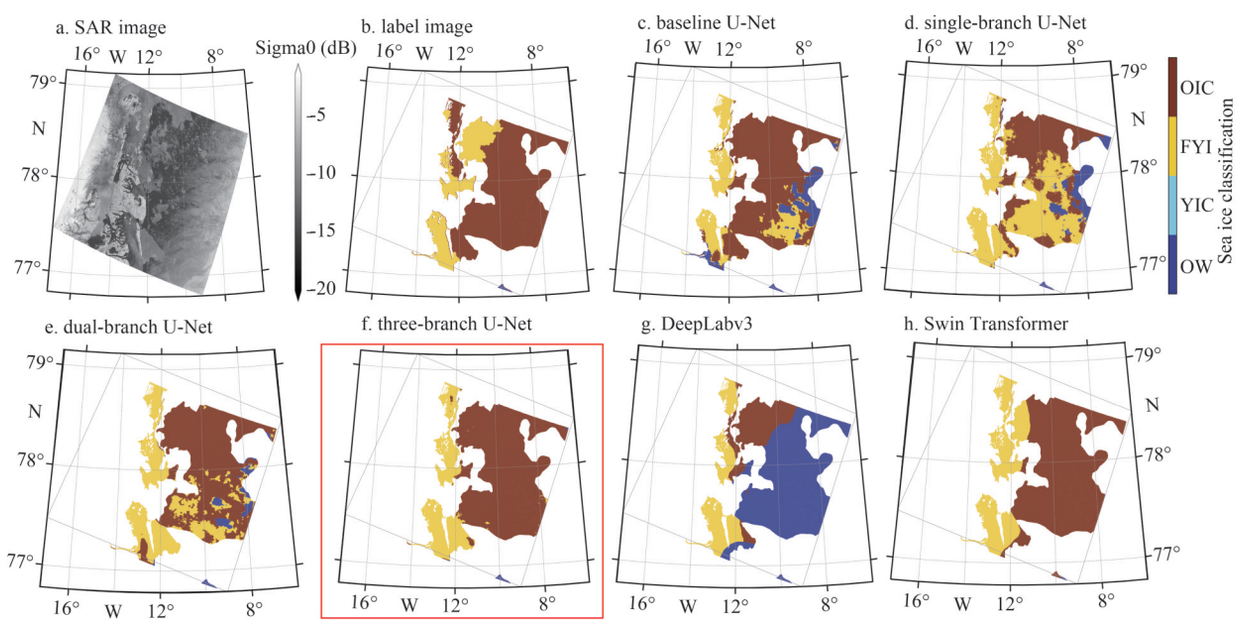

Fig.10 Classification results of different network architectures for scene 20210713T082640_dmi

The red box highlights the result from our proposed model, which achieves the best performance. The corresponding image is also italicized for emphasis.

design, thereby improving the fine-grained multi-classification accuracy of OW, YIC, FYI, and OIC in SAR images. This research offers valuable insights into enhancing the classification and recognition accuracy of sea ice-related objects in SAR images by integrating multimodal information.

5 CONCLUSION

Under the current global climate change scenario, the rapid transformation of Arctic sea ice poses significant challenges to polar ecosystems and the safety of the Arctic shipping route. High-precision sea ice classification provides a critical foundation for understanding sea ice dynamics, supporting climate modeling, and assessing navigation risks. This study proposes a three-branch U-Net model for classifying sea ice in SAR images. By integrating polarimetric information, GLCM feature, and auxiliary data, the model can classify OW, YIC, FYI, and OIC. The model is trained and tested on

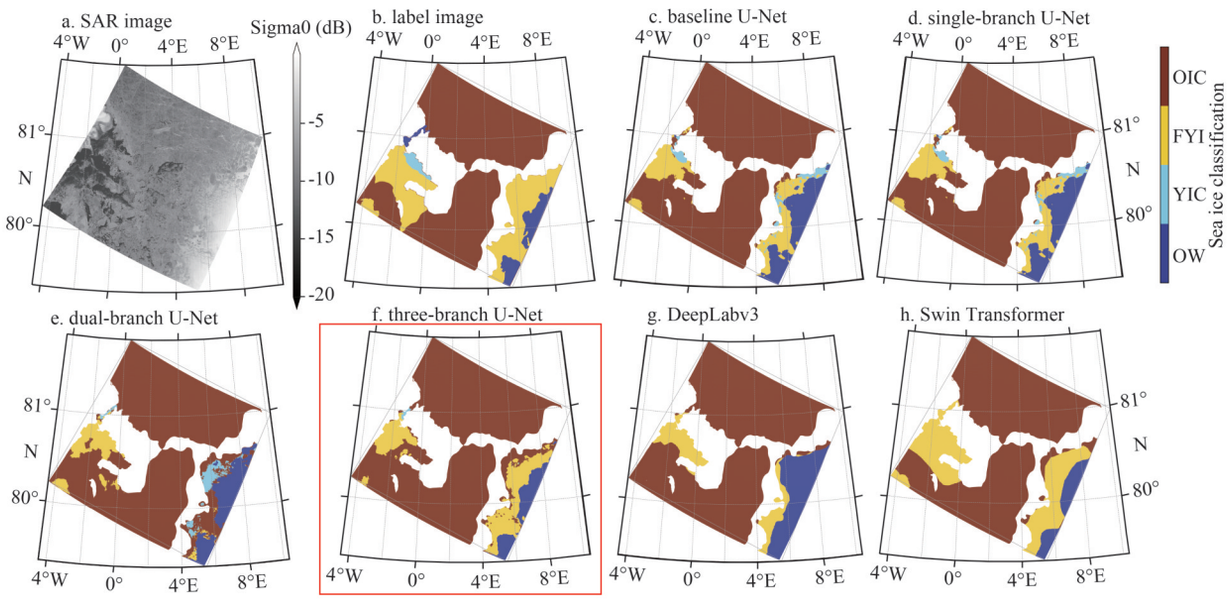

Fig.11 Classification results of different network architectures for scene 20210429T080105_dmi

the well-known AI4Arctic sea ice challenge dataset. Through systematic experimental validation, the following key conclusions are drawn.

First, HV_mean can significantly enhance the accuracy of four-type sea ice classification. Through JM distance analysis of ten GLCM feature parameters, three critical texture features were identified: entropy, variance, and mean. Experimental results demonstrate that HV_mean exhibits superior performance in global classification tasks, achieving a precision of 0.914 5 and an IoU of 0.846 4, significantly outperforming other individual and combined GLCM features. HV_mean offers balanced discriminative capability for YIC, FYI, and OIC, effectively addressing the limitations associated with misclassification that arise from using solely polarimetric SAR information for fine-grained sea ice classification.

Second, the proposed three-branch input structure of the U-Net model is more effective than the single-branch structure in fusing multiple input data. Comparative analysis with the baseline U-Net, single-branch enhanced U-Net, dual-branch U-Net, DeepLabV3, and Swin Transformer demonstrates that the three-branch U-Net achieves optimal multimodal data fusion for fine-grained sea ice classification through independent feature extraction from polarimetric SAR information, GLCM features, and auxiliary data. Experimental results show that the three-branch architecture achieves a precision of 0.914 5 and an IoU of 0.846 4, representing 4.7% and 7% improvements, respectively, over the baseline model. These findings validate the architecture's effectiveness in fusing heterogeneous input modalities, establishing a methodological framework for enhancing SAR-based sea ice object recognition through multimodal information fusion.

Future research will focus on expanding the evaluation of the proposed model by incorporating SAR images from additional Arctic regions to systematically validate its classification performance across diverse sea ice conditions. We will also utilize the proposed three-branch U-Net model to develop a high-resolution sea ice classification dataset covering the entire Arctic region. This dataset will provide valuable support for investigating long-term changes in Arctic sea ice types and enhancing safe Arctic navigation through improved sea ice monitoring and forecasting capabilities.

6 DATA AVAILABILITY STATEMENT

The original AI4Arctic Sea Ice Challenge dataset is free available at https://doi.org/10.11583/DTU.c.6244065.v2. The datasets generated during and/or analyzed during the current study are available from the corresponding author on reasonable request.

References

Alkaee Taleghan S, Barrett A P, Meier W N et al. 2025. IceBench: a benchmark for deep-learning-based sea-ice type classification. *Remote Sensing*, **17**(9): 1646, https://doi.org/10.3390/rs17091646.

Babb D G, Galley R J, Kirillov S et al. 2023. The stepwise reduction of multiyear sea ice area in the arctic ocean

since 1980. *Journal of Geophysical Research*: *Oceans*, **128**(10): e2023JC020157, https://doi.org/10.1029/2023JC020157.

Bi H B, Liang Y, Wang Y H et al. 2020. Arctic multiyear sea ice variability observed from satellites: a review. *Journal of Oceanology and Limnology*, **38**(4): 962-984, https://doi.org/10.1007/s00343-020-0093-7.

Chen X W, Patel M, Pena Cantu F J et al. 2024. MMSeaIce: a collection of techniques for improving sea ice mapping with a multi-task model. *The Cryosphere*, **18**(4): 1621-1632, https://doi.org/10.5194/tc-18-1621-2024.

Chen X W, Patel M, Xu L L et al. 2025. A weakly supervised learning approach for sea ice stage of development classification from AI4 arctic sea ice challenge dataset. *IEEE Transactions on Geoscience and Remote Sensing*, **63**: 4202915, https://doi.org/10.1109/TGRS.2025.3542803.

Comiso J C. 1990. Arctic multiyear ice classification and summer ice cover using passive microwave satellite data. *Journal of Geophysical Research*: *Oceans*, **95**(C8): 13411-13422, https://doi.org/10.1029/JC095iC08p13411.

Comiso J C. 2012. Large decadal decline of the arctic multiyear ice cover. *Journal of Climate*, **25**(4): 1176-1193, https://doi.org/10.1175/JCLI-D-11-00113.1.

Cui Y R, Zou B, Han Z et al. 2020. Application of convolutional neural networks in satellite remote sensing sea ice image classification: a case study of sea ice in the Bohai Sea. *Haiyang Xuebao*, **42**(9): 100-109, https://doi.org/10.3969/j.issn.0253-4193.2020.09.011. (in Chinese with English abstract)

Dabboor M, Geldsetzer T. 2014. Towards sea ice classification using simulated RADARSAT Constellation Mission compact polarimetric SAR imagery. *Remote Sensing of Environment*, **140**: 189-195, https://doi.org/10.1016/j.rse.2013.08.035.

Dawson G, Landy J, Tsamados M et al. 2022. A 10-year record of Arctic summer sea ice freeboard from CryoSat-2. *Remote Sensing of Environment*, **268**: 112744, https://doi.org/10.1016/j.rse.2021.112744.

Fetterer F, Bertoia C, Ye J P. 1997. Multi-year ice concentration from RADARSAT. *In*: Proceedings of IEEE International Geoscience and Remote Sensing Symposium Proceedings. Remote Sensing–A Scientific Vision for Sustainable Development. IEEE, Singapore, Singapore. p.402-404, https://doi.org/10.1109/IGARSS.1997.615897.

Gao L, Li X F, Kong F Z et al. 2022. AlgaeNet: a deep-learning framework to detect floating green algae from optical and SAR imagery. *IEEE Journal of Selected Topics in Applied Earth Observations and Remote Sensing*, **15**: 2782-2796, https://doi.org/10.1109/JSTARS.2022.3162387.

Geldsetzer T, Yackel J, Tomar K S et al. 2023. Melt pond detection on landfast sea ice using dual co-polarized Ku-band backscatter. *Remote Sensing of Environment*, **296**: 113725, https://doi.org/10.1016/j.rse.2023.113725.

Gillioz A, Casas J, Mugellini E et al. 2020. Overview of the transformer-based models for NLP tasks. *In*: Proceedings of 2020 Federated Conference on Computer Science and Information Systems. ACSIS, Sofia, Bulgaria. p.179-183, https://doi.org/10.15439/2020F20.

Hersbach H, Bell B, Berrisford P et al. 2020. The ERA5 global reanalysis. *Quarterly Journal of the Royal Meteorological Society*, **146**(730): 1999-2049, https://doi.org/10.1002/qj.3803.

Holland M M, Bitz C M. 2003. Polar amplification of climate change in coupled models. *Climate Dynamics*, **21**(3): 221-232, https://doi.org/10.1007/s00382-003-0332-6.

Huang J X, Zhang T Y, Cao Y F et al. 2021. The evolution of navigation performance of Northeast Passage under the scenario of Arctic sea ice melting. *Acta Geographica Sinica*, **76**(5): 1051-1064, https://doi.org/10.11821/dlxb202105001. (in Chinese with English abstract)

Huang Y, Ren Y B, Li X F. 2024. Deep learning techniques for enhanced sea-ice types classification in the Beaufort Sea via SAR imagery. *Remote Sensing of Environment*, **308**: 114204, https://doi.org/10.1016/j.rse.2024.114204.

Huang Y, Ren Y B. 2023. A U-Net sea ice classification model based on dual-polarized SAR images. *Oceanologia et Limnologia Sinica*, **54**(6): 1551-1563, https://doi.org/10.11693/hyhz20230300063. (in Chinese with English abstract)

Jiang M Z, Chen X W, Xu L L et al. 2024. IceGCN: an interactive sea ice classification pipeline for SAR imagery based on graph convolutional network. *Remote Sensing*, **16**(13): 2301, https://doi.org/10.3390/rs16132301.

Karvonen J. 2017. Baltic sea ice concentration estimation using SENTINEL-1 SAR and AMSR2 microwave radiometer data. *IEEE Transactions on Geoscience and Remote Sensing*, **55**(5): 2871-2883, https://doi.org/10.1109/TGRS.2017.2655567.

Kwok R. 2018. Arctic sea ice thickness, volume, and multiyear ice coverage: losses and coupled variability (1958-2018). *Environmental Research Letters*, **13**(10): 105005, https://doi.org/10.1088/1748-9326/aae3ec.

Li W, Hsu C Y, Tedesco M. 2024. Advancing Arctic sea ice remote sensing with AI and deep learning: now and future. *EGUsphere*, **2024**: 1-36, https://doi.org/10.3390/rs16203764.

Li X F, Liu B, Zheng G et al. 2020. Deep-learning-based information mining from ocean remote-sensing imagery. *National Science Review*, **7**(10): 1584-1605, https://doi.org/10.1093/nsr/nwaa047.

Li X F, Wang F. 2023. Artificial Intelligence Oceanography. Springer, Singapore, Singapore, https://doi.org/10.1007/978-981-19-6375-9.

Liu H Y, Guo H D, Zhang L. 2015. SVM-based sea ice classification using textural features and concentration from RADARSAT-2 Dual-Pol ScanSAR data. *IEEE Journal of Selected Topics in Applied Earth Observations and Remote Sensing*, **8**(4): 1601-1613, https://doi.org/10.1109/JSTARS.2014.2365215.

Lohse J, Doulgeris A P, Dierking W. 2021. Incident angle dependence of Sentinel-1 texture features for sea ice classification. *Remote Sensing*, **13**(4): 552, https://doi.org/10.3390/rs13040552.

Mori M, Kosaka Y, Watanabe M et al. 2019. A reconciled estimate of the influence of Arctic sea-ice loss on recent Eurasian cooling. *Nature Climate Change*, **9**(2): 123-

129, https://doi.org/10.1038/s41558-018-0379-3.

Park J W, Korosov A A, Babiker M et al. 2020. Classification of sea ice types in Sentinel-1 synthetic aperture radar images. *The Cryosphere*, **14**(8): 2629-2645, https://doi.org/10.5194/tc-14-2629-2020.

Park J W, Won J S, Korosov A A et al. 2019. Textural noise correction for Sentinel-1 TOPSAR cross-polarization channel images. *IEEE Transactions on Geoscience and Remote Sensing*, **57**(6): 4040-4049, https://doi.org/10.1109/TGRS.2018.2889381.

Qu Z F, Su J. 2023. Improved algorithm for determining the freeze onset of Arctic sea ice using AMSR-E/2 data. *Remote Sensing of Environment*, **297**: 113748, https://doi.org/10.1016/j.rse.2023.113748.

Radhakrishnan K, Scott K A, Clausi D A. 2021. Sea ice concentration estimation: using passive microwave and SAR data with a U-Net and curriculum learning. *IEEE Journal of Selected Topics in Applied Earth Observations and Remote Sensing*, **14**: 5339-5351, https://doi.org/10.1109/JSTARS.2021.3076109.

Rantanen M, Karpechko A Y, Lipponen A et al. 2022. The Arctic has warmed nearly four times faster than the globe since 1979. *Communications Earth & Environment*, **3**(1): 168, https://doi.org/10.1038/s43247-022-00498-3.

Reichstein M, Camps-Valls G, Stevens B et al. 2019. Deep learning and process understanding for data-driven Earth system science. *Nature*, **566**(7743): 195-204, https://doi.org/10.1038/s41586-019-0912-1.

Ren Y B, Li X F, Yang X F et al. 2022. Development of a dual-attention U-Net model for sea ice and open water classification on SAR images. *IEEE Geoscience and Remote Sensing Letters*, **19**: 4010205, https://doi.org/10.1109/LGRS.2021.3058049.

Sen R, Goswami S, Chakraborty B. 2019. Jeffries-Matusita distance as a tool for feature selection. *In*: Proceedings of 2019 International Conference on Data Science and Engineering. IEEE, Patna, India. p.15-20, https://doi.org/10.1109/ICDSE47409.2019.8971800.

Serreze M C, Barry R G. 2011. Processes and impacts of Arctic amplification: a research synthesis. *Global and Planetary Change*, **77**(1-2): 85-96, https://doi.org/10.1016/j.gloplacha.2011.03.004.

Soh L K, Tsatsoulis C, Gineris D et al. 2004. ARKTOS: an intelligent system for SAR sea ice image classification. *IEEE Transactions on Geoscience and Remote Sensing*, **42**(1): 229-248, https://doi.org/10.1109/TGRS.2003.817819.

Soh L K, Tsatsoulis C. 1999. Texture analysis of SAR sea ice imagery using gray level co-occurrence matrices. *IEEE Transactions on Geoscience and Remote Sensing*, **37**(2): 780-795, https://doi.org/10.1109/36.752194.

Stokholm A, Buus-Hinkler J, Wulf T et al. 2024. The AutoICE challenge. *The Cryosphere*, **18**(8): 3471-3494, https://doi.org/10.5194/tc-18-3471-2024.

Su H, Ji B W, Wang Y P. 2019. Sea ice extent detection in the Bohai Sea using Sentinel-3 OLCI Data. *Remote Sensing*, **11**(20): 2436, https://doi.org/10.3390/rs11202436.

Su H, Wang Y P, Xiao J et al. 2013. Improving MODIS sea ice detectability using gray level co-occurrence matrix texture analysis method: a case study in the Bohai Sea. *ISPRS Journal of Photogrammetry and Remote Sensing*, **85**: 13-20, https://doi.org/10.1016/j.isprsjprs.2013.07.010.

Walker N P, Partington K C, van Woert M L et al. 2006. Arctic sea ice type and concentration mapping using passive and active microwave sensors. *IEEE Transactions on Geoscience and Remote Sensing*, **44**(12): 3574-3584, https://doi.org/10.1109/TGRS.2006.881116.

Wang H Y, Li X F. 2024a. DeepBlue: advanced convolutional neural network applications for ocean remote sensing. *IEEE Geoscience and Remote Sensing Magazine*, **12**(1): 138-161, https://doi.org/10.1109/MGRS.2023.3343623.

Wang H Y, Li X F. 2024b. Expanding horizons: U-Net enhancements for semantic segmentation, forecasting, and super-resolution in ocean remote sensing. *Journal of Remote Sensing*, **4**: 0196, https://doi.org/10.34133/remotesensing.0196.

Wang L, Scott K A, Xu L L et al. 2016. Sea ice concentration estimation during melt from Dual-Pol SAR scenes using deep convolutional neural networks: a case study. *IEEE Transactions on Geoscience and Remote Sensing*, **54**(8): 4524-4533, https://doi.org/10.1109/TGRS.2016.2543660.

Wang Y H, Bi H B, Huang H J et al. 2019. Satellite-observed trends in the Arctic sea ice concentration for the period 1979-2016. *Journal of Oceanology and Limnology*, **37**(1): 18-37, https://doi.org/10.1007/s00343-019-7284-0.

Xu H, Ren Y B. 2021. Detecting sea ice of Bohai Sea using SAR images based on a hybrid loss U-Net model. *Haiyang Xuebao*, **43**(6): 157-170, https://doi.org/10.12284/hyxb2021084. (in Chinese with English abstract)

Ye Y F, Heygster G, Shokr M. 2016. Improving multiyear ice concentration estimates with reanalysis air temperatures. *IEEE Transactions on Geoscience and Remote Sensing*, **54**(5): 2602-2614, https://doi.org/10.1109/TGRS.2015.2503884.

Zakhvatkina N Y, Alexandrov V Y, Johannessen O M et al. 2013. Classification of sea ice types in ENVISAT synthetic aperture radar images. *IEEE Transactions on Geoscience and Remote Sensing*, **51**(5): 2587-2600, https://doi.org/10.1109/TGRS.2012.2212445.

Zhang X, Dierking W, Zhang J et al. 2016. Retrieval of the thickness of undeformed sea ice from simulated C-band compact polarimetric SAR images. *The Cryosphere*, **10**(4): 1529-1545, https://doi.org/10.5194/tc-10-1529-2016.

Zhang X, Zhang J, Meng J M et al. 2013. Analysis of multi-dimensional SAR for determining the thickness of thin sea ice in the Bohai Sea. *Chinese Journal of Oceanology and Limnology*, **31**(3): 681-698, https://doi.org/10.1007/s00343-013-2057-7.

Zhang X, Zhu Y X, Zhang J et al. 2021. Assessment of arctic sea ice classification ability of Chinese HY-2B dual-band radar altimeter during winter to early spring conditions. *IEEE Journal of Selected Topics in Applied Earth Observations and Remote Sensing*, **14**: 9855-9872, https://doi.org/10.1109/JSTARS.2021.3114228.

Zhao L, Xie T, Perrie W et al. 2023. Deep-learning-based sea ice classification with Sentinel-1 and AMSR-2 data. *IEEE Journal of Selected Topics in Applied Earth Observations and Remote Sensing*, **16**: 5514-5525, https://doi.org/10.1109/JSTARS.2023.3285857.